Broadband dielectric spectroscopy of phonons and polar nanoclusters in $PbMg_{1/3}Nb_{2/3}O_3$-35%$PbTiO_3$ ceramics: Grain size effects

V. Bovtun,[1] S. Kamba,[1,*] S. Veljko,[1] D. Nuzhnyy,[1] J. Kroupa,[1] M. Savinov,[1] P. Vaněk,[1] J. Petzelt,[1] J. Holc,[2] M. Kosec,[2] H. Amorín,[3] and M. Alguero[3]

[1]*Institute of Physics ASCR, v.v.i. Na Slovance 2, 18221 Prague, Czech Republic*

[2]*Institute Jozef Stefan, Jamova 39, 1000 Ljubljana, Slovenia*

[3]*Instituto de Ciencia de Materiales de Madrid, CSIC, Cantoblanco, 28049 Madrid, Spain*

(Received 27 November 2008; revised manuscript received 17 February 2009; published 25 March 2009)

The dielectric response of $PbMg_{1/3}Nb_{2/3}O_3$-35%$PbTiO_3$ ceramics (close to the morphotropic phase boundary) from 100 Hz up to 100 THz was determined in a broad temperature range of 5–900 K. Two ceramics were studied and compared: coarse grain ceramics (CGC) (grain size ~4 μm) and fine grain ceramics (FGC) (grain size ~150 nm). Both ceramics showed similar polar-phonon response and the ferroelectric transition near T_C=440 K that was manifested by partial softening of the overdamped lowest-frequency phonon using the time-domain THz spectroscopy. However, the dielectric response was dominated by a complex relaxational dispersion in the microwave range due to relaxorlike dynamics of the polar nanoclusters, which strongly differed in both the ceramics. Whereas the CGC undergoes a well-defined ferroelectric transition such as a single crystal, FGC exhibits a relaxor behavior with substantially smaller permittivity showing partial clamping of the polar nanocluster dynamics by grain boundaries. The pronounced difference was also revealed in a second-harmonic generation showing much larger paraelectric signal in the FGC with a much smeared ferroelectric transition only. Due to contributions of both the soft phonon mode and dielectric relaxations into the dielectric constant near its maximum even in the paraelectric phase, the ferroelectric transition corresponds to a percolation threshold of the polar nanoclusters into macroscopic domains. Such a type of phase transition can be considered as a special case of crossover between the displacive and order-disorder types, where the ordering process concerns a mesoscopic range.

DOI: 10.1103/PhysRevB.79.104111 PACS number(s): 77.22.−d, 78.30.−j, 63.20.−e

I. INTRODUCTION

In the last decade we have witnessed massive application of ferroelectric (FE) components in microelectronics. The most attractive are the applications of FE materials in multilayer capacitors (based on $BaTiO_3$), FE random access memories (mainly out of $PbZr_{1-x}Ti_xO_3$ and $SrBi_2Ti_2O_9$), and piezoelectric components (based mainly on $PbZr_{1-x}Ti_xO_3$). Unfortunately, it was shown that the FE properties (permittivity ε', spontaneous polarization P_s, Curie temperature T_C, etc.) deteriorate with the reduced thickness of the FE films and with decreasing size of the ceramic grains (for size effect, see the review[1]). Understanding the size effect in FE materials became the interest of many physicists and material scientists. Up to now, many contradictory theoretical and experimental results have appeared on the critical size for ferroelectricity and about the reasons of the reduced ε', P_s, and T_C. Several influences, both extrinsic and intrinsic, have been considered. They arise from strain, chemical, and structural defects in the crystal lattice (e.g., oxygen vacancies), dead (low-permittivity) interfacial layers, grain boundaries in ceramics and polycrystalline films, etc.

The size effect was mostly investigated for $BaTiO_3$ since the modern multilayer capacitors with layer thicknesses below 1 μm require the $BaTiO_3$ grain size of the order of 100 nm, in which large reduction in ε' was observed. It was shown that mainly extrinsic effects play the role in reduction in ε' and P_s, as well as in smearing and shifts of the dielectric anomalies. Study of a nanosized $BaTiO_3$ single-crystal capacitor (thickness ~75 nm) demonstrated a dielectric anomaly as sharp as in the bulk showing that the extrinsic contributions can be eliminated.[2] Several theoretical papers estimated the critical thickness of six, four, or even three unit cells for the appearance of ferroelectricity.[3] Some papers show that the boundary conditions (electrodes, other dielectric layers on the thin-film surface, etc.) can help to stabilize the FE phase so that the FE phase was observed in films with thicknesses down to three[4] or even one unit cell.[5]

Concerning the influence of grain size on ε', substantially lower ε' is commonly observed in thin films compared to single crystals. Also many bulk ceramics exhibit reduced ε' and it was shown that mainly grain boundaries of low local ε' play the role in it.[6] This effect is especially remarkable in high-permittivity materials such as $SrTiO_3$ (at low temperatures), where dramatic decrease in ε' was observed with reducing the grain size.[7,8]

Giant ε' exists also in bulk relaxor ferroelectrics (RFE). These materials are not necessary FEs at low temperatures but they exhibit broad maximum of $\varepsilon'(T)$ at temperature T_{max} which is strongly frequency dependent: T_{max} remarkably increases and ε'_{max} decreases with increasing frequency. These properties were explained by dynamics of polar nanoregions or nanoclusters (PNC), which appear typically up to ~300 K above T_m (T_m is T_{max} at low frequencies) at so-called Burns temperature T_B.[9] The clusters are dynamic below T_B (Ref. 10) but probably they become quasistatic 100–200 K below T_B at so-called T^* temperature.[11–14] The size and concentration of clusters increases on cooling below T^* and PNC finally freeze out at the freezing temperature T_f or jumpwise increase into macroscopic FE domains below T_C.[15]

Dielectric relaxation related to the PNC dynamics appears in addition to the polar-phonon response below T_B in the THz range (overlapping with the phonon response), slows down, and anomalously broadens on cooling (sometimes even splits) giving rise to almost uniform distribution of relaxation frequencies below T_f responsible for the pronounced frequency-independent dielectric losses below T_f.[16–18]

The optical phonons and their temperature behavior in $[PbMg_{1/3}Nb_{2/3}O_3]_{1-x}$-$[PbTiO_3]_x$ (PMN-PT) were studied mainly by Raman scattering[19–22] and only at selected temperatures by Fourier transform infrared (FTIR) reflectivity.[20] However, the low-frequency modes were not fully resolved due to their overdamping and no softening near T_C was revealed. The difficulties and ambiguities in evaluating the overdamped low-frequency Raman response was carefully analyzed by Toulouse *et al.*[11] for the case of the $Pb(Zn_{1/3}Nb_{2/3})O_3$ single-crystal relaxor. Acoustic and the lowest energy optical phonon branches were also investigated by means of inelastic neutron scattering (INS).[23,24] However, TO1 phonons with small wave vector near Brillouin zone were not resolved in the INS spectra between T_B and 200 K (Ref. 23) because of their overdamping and so-called phonon waterfall effect (merging of optical and acoustic branches).[25] In this work we, however, report on splitting of TO1 phonon and on appreciable phonon softening of its lowest energy component near T_C revealed using the time-domain THz spectroscopy.

Enhanced interest on the physics and technology of RFE rose after the work of Park and Shrout,[26] who discovered one order-of-magnitude stronger piezoelectric effect (in comparison with at that time best piezoelectric $PbZr_{1-x}Ti_xO_3$ ceramics) in the single-crystal solid solution of typical RFE $PbMg_{1/3}Nb_{2/3}O_3$ (as well as $PbZn_{1/3}Nb_{2/3}O_3$) and classical FE $PbTiO_3$. The best piezoelectric properties of PMN-PT were observed for the PT concentration close to the morphotropic phase boundary (MPB) ($x=0.33$) between the tetragonal and rhombohedral phases. Giant piezoelectric response was explained by an easy rotation of polarization in the monoclinic phase close to MPB (Refs. 27 and 28); however the recent theoretical[29,30] and experimental[31] studies revealed no monoclinic phase near MPB but the coexistence of rhombohedral and tetragonal nanodomains, in which the polarization can be easily rotated.[29]

Size effect in RFE and piezoelectrics was much less investigated than in classical FEs. Nevertheless, it can be expected that the same trend of miniaturization as in multilayer capacitors will occur in multilayer ceramic actuators, and the problem of grain size influence on the dielectric and piezoelectric properties will become highly actual. Several papers concerned the grain size influence on ε' and crystal structure in PMN (Ref. 32) and PMN-PT.[33–36] However, all these papers refer only to dielectric response below 1 MHz. No studies of PMN and PMN-PT ceramics with different grain size were performed in the microwave (MW), THz, and infrared (IR) ranges, not speaking of high temperatures near and above T_B although the high-frequency response and its evolution with temperature is needed for understanding the huge low-frequency ε' and dynamics of the ferroelectric phase transitions.

Only in the case of PMN was the dielectric response of single crystal, ceramics, and thin films compared in a broad spectral range.[18] Actually, two to three times lower ε'_m (ε'_m is maximum permittivity at the lowest measured frequencies) in PMN ceramics and almost ten times lower ε'_m in thin films compared to PMN single crystal was observed and explained by different dynamics of PNC in confined ceramic grains and thin films, which leads to higher relaxation frequency and lower dielectric strength. Also the FE soft-mode (SM) doublet was observed in the THz and IR spectra, whose A_1 component partially softened on heating to T_B and the E component appeared quite soft, below 1 THz, at all temperatures below T_B. SM is split due to the locally broken noncubic symmetry in PNC although the macroscopic symmetry remains cubic at all temperatures. The frequencies of both SM components did not differ among all the samples, i.e., the phonon dynamics is not sensitive to the size of the grain, only the dielectric relaxation (PNC dynamics) is strongly affected by the available dimensions.

The aim of this paper is to report on the study of broadband (10^2–10^{14} Hz) dielectric spectra of PMN-PT ($x=0.35$) ceramics near MPB with the giant piezoelectric response. PMN-PT ($x=0.35$) exhibits two successive phase transitions on cooling, from cubic to tetragonal and rhombohedral phase, but also a strong relaxor behavior in the paraelectric phase. Besides studying the phonon behavior and its temperature dependence, of interest is also the influence of the fine grain structure on the relaxor dielectric response, on the dynamics of PNCs and on both FE transitions in PMN-PT. Therefore the dielectric response of the coarse and fine grain ceramics were compared in a broad temperature range. Dielectric data were complemented by a second-harmonic generation (SHG) experiment which is sensitive also to local breaking of the center of symmetry expected in PNC below T_B.

II. EXPERIMENTAL

Two kinds of the PMN-PT ($x=0.35$) ceramics with different grain structure were prepared and studied. Fine grain ceramics (FGC) with the average grain size ~150 nm and ~97% theoretical density were prepared from the nanocrystalline powder by hot pressing.[37] Coarse grain ceramics (CGC) with the average grain size ~4 μm and ~92% theoretical density were prepared from the same nanocrystalline powder by sintering in a PbO atmosphere.[37]

Complex dielectric response $\varepsilon^*=\varepsilon'-i\varepsilon''$ of both ceramics was studied between 5 and 900 K in the frequency range from 100 Hz to 100 THz. Several experimental techniques were used to cover such a broad spectral range. The low-frequency dielectric properties were measured in the 100 Hz–1 MHz range using a HP 4192A impedance analyzer with a Leybold He-flow cryostat (operating range of 5–300 K) and a custom-made furnace (300–900 K). Dielectric measurements in the high-frequency range (1 MHz–1.8 GHz) were performed using a computer-controlled dielectric spectrometer equipped with a HP 4291B impedance analyzer, Novocontrol BDS 2100 coaxial sample cell, and Sigma System M18 temperature chamber (operating range of 100–500 K). The dielectric parameters were calculated taking into account the electromagnetic field distribution in the sample.

MW dielectric properties were measured at 8.8 GHz using the TE_{0n1} composite dielectric resonator,[38] vector network analyzer Agilent E8364B, and Sigma System M18 temperature chamber (100–380 K). Time-domain THz transmission spectra were obtained using a laboratory-made spectrometer based on an amplified Ti-sapphire femtosecond laser system. Two ZnTe crystal plates were used to generate (by optic rectification) and to detect (by electro-optic sampling) the THz pulses. Both the transmitted field amplitude and phase shift were simultaneously measured which allowed us to determine directly the complex dielectric response $\varepsilon^*(\omega)$ in the range from 3 to 35 cm^{-1} (100 GHz–1 THz) at temperatures from 5 to 800 K. An Optistat (Oxford Inst.) continuous flow cryostat with mylar windows was used for cooling, and a commercial high-temperature cell SPECAC P/N 5850 for the heating. The samples are highly absorbing in the THz range; therefore thin plates with thickness of 43 μm (diameter ~8 mm) were investigated. IR reflectivity spectra were obtained using the FTIR spectrometer Bruker IFS 113v in the frequency range of 20–3300 cm^{-1} (0.6–100 THz) at temperatures of 5–800 K. The same furnace and cryostat as for the THz spectrometer were used but with polyethylene windows instead of mylar ones for the cryostat.

Temperature dependences of the dielectric parameters at low, high, and MW frequencies were measured during slow cooling with a temperature rate of 1–2 K/min, if not extra specified. THz and IR spectra were taken at the fixed stabilized temperatures with intervals of 25–50 K.

Differential scanning calorimetry (DSC) measurements were performed on Perkin-Elmer Pyris-Diamond DSC calorimeter in the temperature range of 100–600 K with a temperature rate of 10 K/min.

SHG was studied in the reflection geometry in the temperature range of 300–750 K. Q-switched Nd-yttrium aluminum garnet laser served as a light source while SHG signal at 532 nm was detected using a photomultiplier followed by a boxcar integrator. Samples were placed in an oven allowing continuous temperature change (2–3 K/min) from 300 K up to 750 K.

III. RESULTS AND ANALYSIS

$\varepsilon'(T)$ of CGC (see Fig. 1) shows a sharp maximum corresponding to the FE phase transition at T_C=440 K and an additional anomaly at T_{TR}=270–290 K revealing the tetragonal-rhombohedral phase transition. Temperature hysteresis (~5 K) of $\varepsilon'(T)$ observed between zero-field heating and cooling as well as the endothermic DSC peak on heating (not shown) indicate the first-order FE phase transition at T_C. On the other hand, dielectric relaxation, revealed near and above T_C in the 1 MHz–1 THz range, is characteristic of RFE.[10] Dielectric dispersion is less pronounced in the FE phase below T_{TR}. The data in Fig. 1 obtained with CGC are qualitatively the same as the data obtained from a single crystal;[39] only the value of ε' is slightly lower, apparently due to the 8% porosity of our ceramics.

$\varepsilon'(T)$ of the FGC (see Fig. 2) shows no sharp anomalies which could be attributed to phase transitions but only typical RFE response is seen, i.e., a diffuse $\varepsilon'(T)$ maximum at

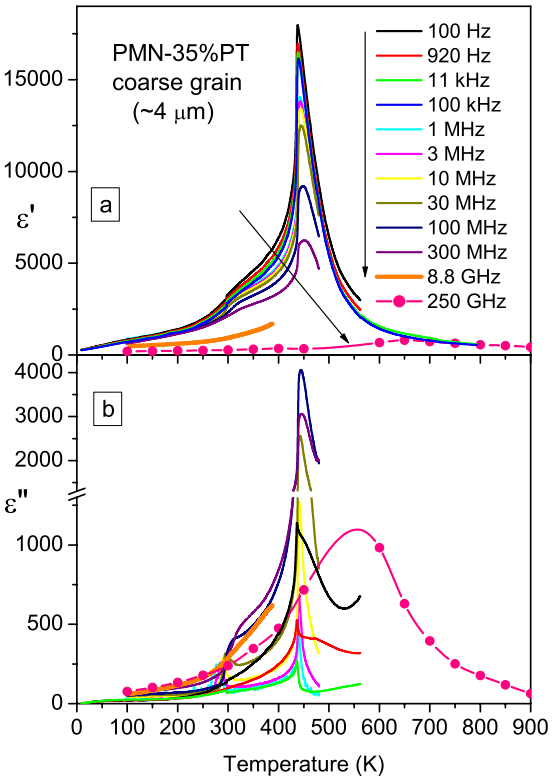

FIG. 1. (Color online) Temperature dependences of (a) dielectric permittivity ε' and (b) loss ε'' of the CGC for frequencies between 100 Hz and 250 GHz.

$T_m \approx 430$ K and a broad relaxational dielectric dispersion both below and above T_m. No DSC anomaly was observed in FGC.

Low-frequency maxima of $\varepsilon'(T)$ in both CGC and FGC undergo a strong dielectric dispersion of relaxational character. Below we will determine the contributions of phonons and dielectric relaxations to the dielectric permittivity.

Let us compare the dielectric properties of CGC and FGC. Low-frequency permittivity [100 Hz, Fig. 3(a)] of FGC at T_m is about three times smaller than that of CGC at T_C while the high-frequency permittivity [300 MHz, Fig. 3(c)] is only by 25% smaller. The maximum loss values of FGC are much smaller than those of CGC both at low and high frequencies [Figs. 3(b) and 3(d)]. The values and shape of the THz $\varepsilon'(T)$ and $\varepsilon''(T)$ curves in both the samples are very similar [250 GHz, Figs. 3(e) and 3(f)], only in FGC are their peaks slightly shifted to lower temperatures. Below T_{TR}, i.e., at temperatures corresponding to the rhombohedral phase in CGC, there is no essential difference between CGC and FGC at any frequency. The features mentioned above show similarity of the high-frequency polarization mechanisms in both ceramics but show more pronounced low-frequency polarization mechanisms and stronger contributions of the PNC dynamics to the permittivity in CGC. The main dielectric dispersion in both the ceramics takes place in the MW range, similar to PZN-8%PT single crystals.[40]

Broadband dielectric spectra of CGC (Fig. 4) reveal two relaxation regions $R1$ and $R2$ between 1 MHz and 1 THz. These relaxations partially slow down on cooling but do not

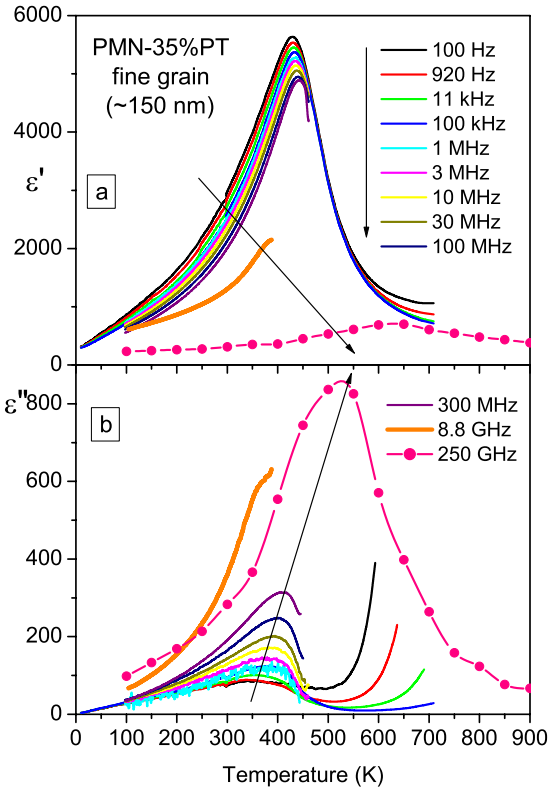

FIG. 2. (Color online) Temperature dependences of (a) dielectric permittivity ε' and (b) loss ε'' of the FGC at frequencies between 100 Hz and 250 GHz.

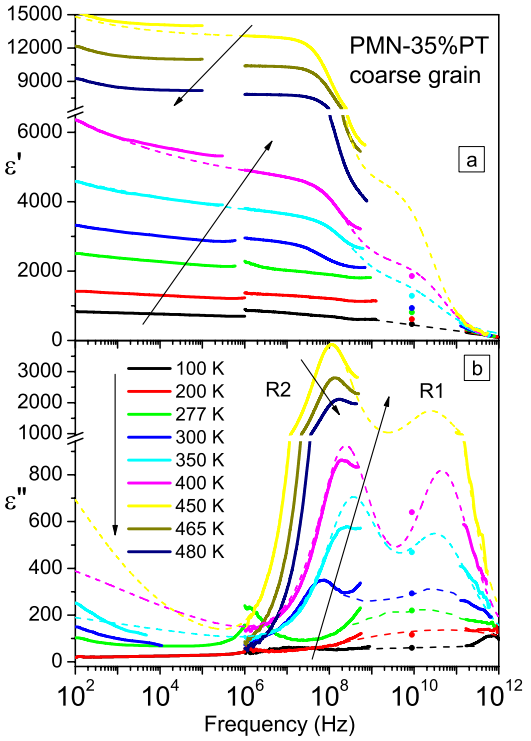

FIG. 4. (Color online) Frequency dependences of (a) dielectric permittivity ε' and (b) loss ε'' of the CGC at temperatures between 100 and 480 K. Dash lines at $T \geq 300$ K are multicomponent Cole-Cole fits. $R1$ and $R2$ denote loss maxima of the two relaxational contributions (see the text).

shift below 1 MHz, unlike in PMN and other RFEs without phase transitions.[10,16,18] The relaxations are weak and very broad below T_{TR}, and nearly frequency-independent dielectric losses are observed below 200 K. Presence of two relaxational contributions ($R1$ and $R2$) in the dielectric response of CGC at $T > T_{TR}$ is clearly seen from the observed peaks of $\varepsilon''(f)$ and from the multicomponent Cole-Cole fits (dash lines at $T \geq 300$ K in Fig. 4). For the detailed analysis we used the empirical Cole-Cole equation with three relaxational contributions:

$$\varepsilon^*(f) = \varepsilon'(f) - i\varepsilon''(f) = \varepsilon_\infty + \sum_{j=1}^{3} \frac{\Delta\varepsilon_j}{1 + (if/\nu_{Rj})^{1-\alpha_j}}, \qquad (1)$$

where $\Delta\varepsilon_j$ is the contribution of the relaxation to the static permittivity (dielectric strength), ε_∞ is the contribution of the

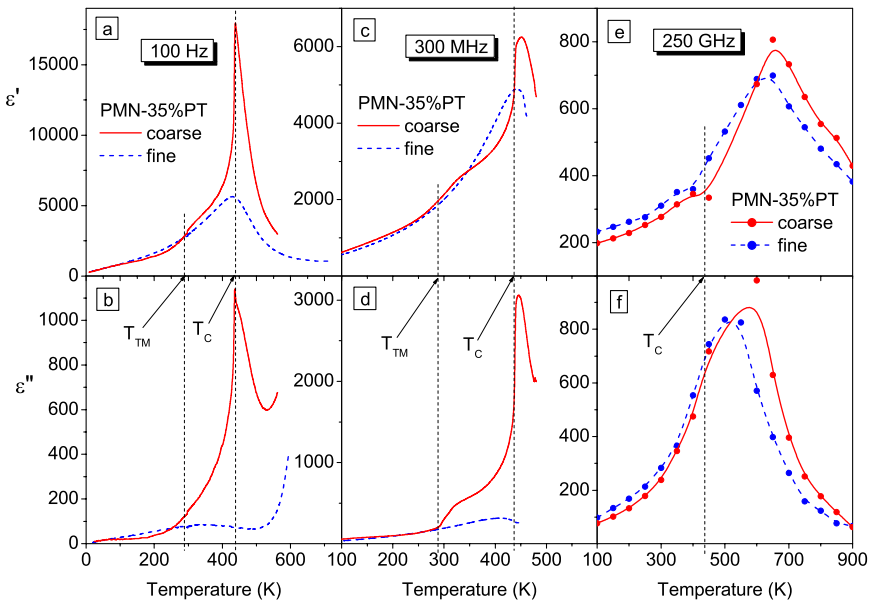

FIG. 3. (Color online) Temperature dependences of the [(a), (c), and (e)] dielectric permittivity ε' and [(b), (d), and (f)] loss ε'' of the CGC (solid lines) and FGC (dash lines) at [(a) and (b)] 100 Hz, [(c) and (d)] 300 MHz, and [(e) and (f)] 250 GHz.

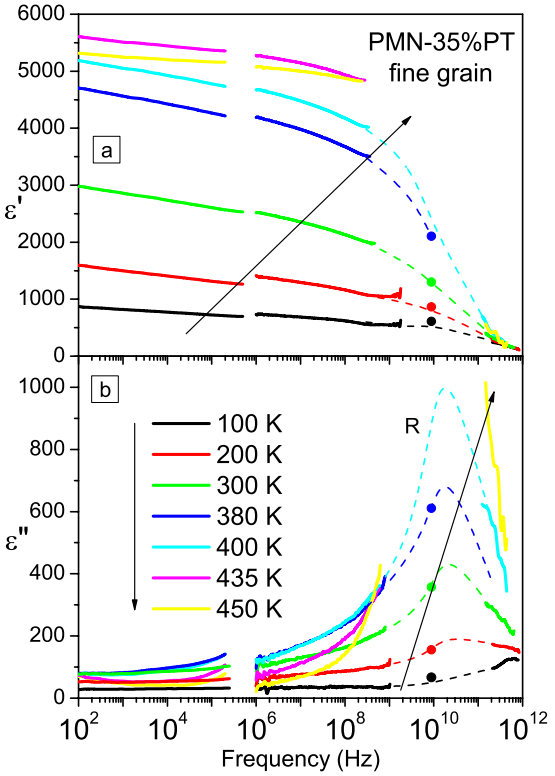

FIG. 5. (Color online) Frequency dependences of (a) dielectric permittivity ε' and (b) loss ε'' of the FGC at temperatures between 100 and 450 K. R denotes the asymmetric loss maximum by two overlapping relaxational contributions (see the text).

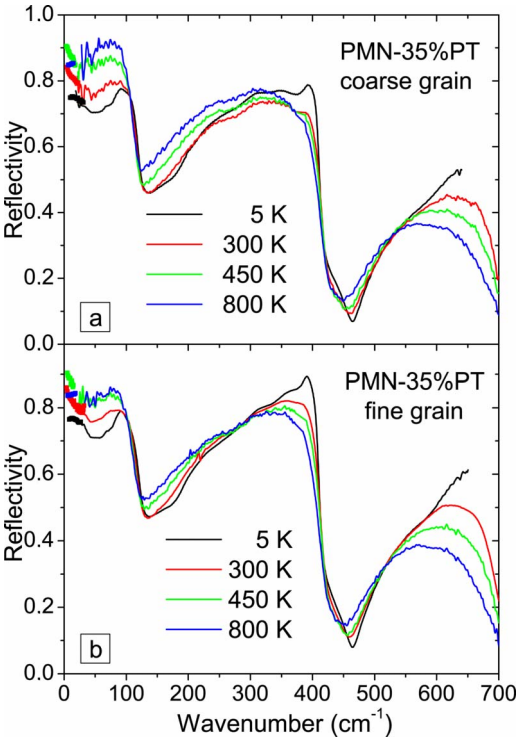

FIG. 6. (Color online) IR and THz reflectivity spectra of (a) CGC and (b) FGC at temperatures between 5 and 800 K. THz reflectivities were calculated from the THz dielectric response.

phonon modes and higher-frequency electronic processes to permittivity, f is the frequency, and ν_{Rj} is the mean relaxation frequency of the jth relaxation. Parameter $0 \leq \alpha_j \leq 1$ characterizes the distribution of relaxation times. The lowest-frequency relaxation $R3$ is present only at high temperatures and low frequencies below 10 kHz. It could be caused by oxygen vacancies but some authors interpreted it as due to a dynamics of PNC.[41] Its mean relaxation frequency ν_{R3} lies below our frequency range and was evaluated in details by other authors.[41] In the subsequent discussion below we will focus on evaluation of the two higher-frequency (above 1 MHz) relaxation processes only, describing in our opinion the PNC dynamics.

The dielectric spectra of FGC (Fig. 5) reveal only one dielectric relaxation [or peak in $\varepsilon''(f)$] in the THz-MW region, which partially slows down and broadens on cooling. Below 100 K the relaxation is weak and nearly frequency-independent dielectric losses are observed. The two relaxational contributions $R1$ and $R2$ cannot be unambiguously determined from the dielectric spectra of FGC but they are recognizable via the asymmetric shape of the $\varepsilon''(f)$ peaks marked as R in Fig. 5(b). The relaxation appears mainly above 10 MHz (i.e., at higher frequencies than in CGC) which is responsible for the lower dielectric strength of this relaxation and the resulting lower ε' of FGC at low frequencies.

For the detailed analysis of the temperature evolution of relaxation frequencies, also the THz and IR spectra are needed because the relaxation shifts up to the THz region at high temperatures. THz spectra above 200 GHz are shown in Figs. 4 and 5 while the IR reflectivity spectra in Fig. 6. The reflectivities $R(\omega)$ below 1 THz were calculated from the complex THz permittivity spectra $\varepsilon^*(\omega)$ using the formula

$$R(\omega) = \left| \frac{\sqrt{\varepsilon^*(\omega)} - 1}{\sqrt{\varepsilon^*(\omega)} + 1} \right|^2. \quad (2)$$

The shape of the IR spectra is very similar to the spectra of pure PMN (Ref. 42) and PMN-27%PT (Ref. 20) crystals or PZN-PMN-PSN ceramics.[43] The IR spectra of CGC and FGC are similar, with the reflectivity of CGC [Fig. 6(a)] being slightly lower presumably because of its lower density. It causes higher diffuse scattering of the reflected IR beam (rising with frequency) and a lower reflectance above 200 cm^{-1} in the less dense ceramics.

IR reflectivity and THz dielectric spectra were fitted simultaneously using Eq. (2), and a generalized oscillator model with the factorized form of the complex permittivity

$$\varepsilon^*(\omega) = \varepsilon_\infty \prod_{j=1}^{n} \frac{\omega_{\mathrm{LO}j}^2 - \omega^2 + i\omega\gamma_{\mathrm{LO}j}}{\omega_{\mathrm{TO}j}^2 - \omega^2 + i\omega\gamma_{\mathrm{TO}j}}. \quad (3)$$

Here $\omega_{\mathrm{TO}j}$ and $\omega_{\mathrm{LO}j}$ mark the transverse and longitudinal angular frequencies of the jth mode, respectively, and $\gamma_{\mathrm{TO}j}$ and $\gamma_{\mathrm{LO}j}$ denote their corresponding damping constants. The high-frequency permittivity ε_∞ has its origin in electronic absorption processes at much higher frequencies than phonon frequencies (typically in UV-VIS range) and it was obtained from the frequency-independent room-temperature reflectivity above the phonon frequencies. The temperature

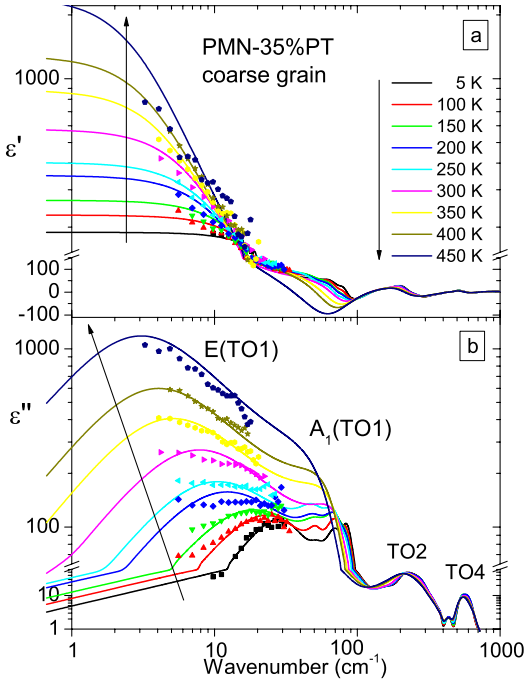

FIG. 7. (Color online) Complex dielectric response of CGC in the THz and IR ranges (solid lines) obtained by fitting of the IR reflectivity spectra together with THz experimental data (symbols) at temperatures below 450 K. TO1, TO2, and TO4 denote the loss maxima attributed to the three IR-active transverse optical phonons. A_1(TO1) and E(TO1) are components of the soft TO1 mode.

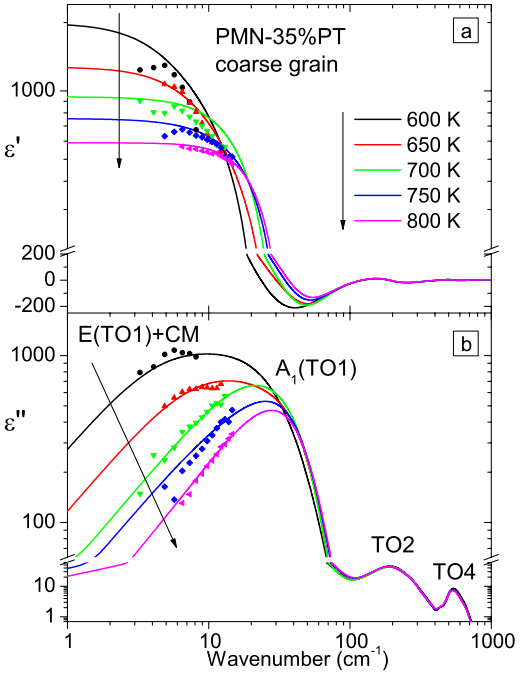

FIG. 8. (Color online) The same as in Fig. 7 for temperatures above 600 K. E(TO1)+CM denotes a joint contribution of the E component and relaxational CM at the lowest frequencies.

dependence of ε_∞ is usually very small and was neglected in our fits.

The real and imaginary parts of $\varepsilon^*(\omega)$ obtained from the fits of IR and THz spectra of CGC and FGC are shown together with the experimental THz data in Figs. 7–10. ε' and ε'' values increase in the THz range on heating up to 450 K (close to T_C) but on further heating they decrease. Therefore for clarity we plotted the ε^* spectra of each sample in two figures (below and above 450 K).

Three main reflection bands characteristic for the simple-cubic paraelectric perovskite structure [TO1, TO2, and TO4 modes (TO3 is silent)] with $Pm\bar{3}m$ space group are seen in the IR reflectivity (Fig. 6) as well as in $\varepsilon''(\omega)$ spectra of both ceramics (Figs. 7–10). Actually seven oscillators were necessary for the fit of paraelectric phase at 800 K (Table I). Such a number of IR-active phonons cannot be expected from the factor group analysis of $Pm\bar{3}m$ or $Fm\bar{3}m$ (Z=2) paraelectric phase, where only three and four IR-active modes are allowed, respectively. But one could assume splitting of modes in the $Fm\bar{3}m$ structure due to chemical inhomogeneities in the perovskite B sublattices (for details see Ref. 44). 13 modes were used for the fit of IR spectra in FE phase at 5 K, which corresponds to the rhombohedral structure with 1:1 short-range order in the B-perovskite site, where 16 IR-active modes are permitted.[44] The phonon spectra and their evolution with temperature are, nevertheless, very similar in both kinds of ceramics (see, e.g., the modes below 100 cm^{-1} in Fig. 11).

The lowest-frequency reflection band below 100 cm^{-1} is due to the TO1 phonon which plays the role of the FE SM and describes mainly the vibration of Pb cations against the BO_6 octahedra framework (so-called Last mode[45]). This band is actually split into two components of A_1(TO1) and E(TO1) symmetries (see Fig. 11) not only below T_C due to the rhombohedral symmetry but also due to the local uniaxial

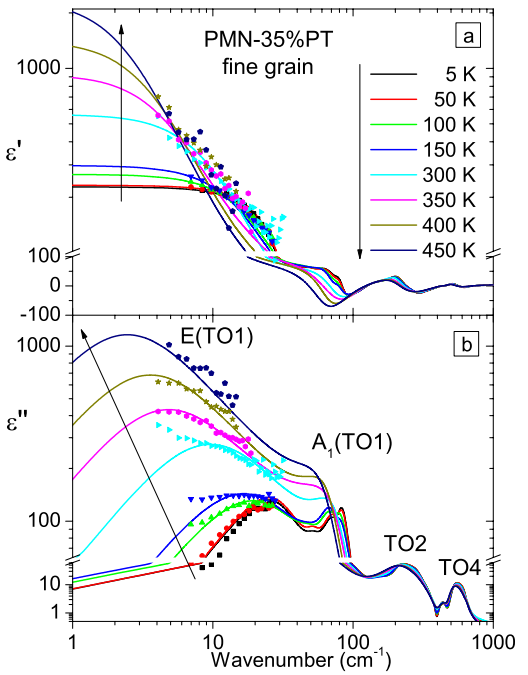

FIG. 9. (Color online) Complex dielectric response of the FGC in the THz and IR ranges (solid lines) obtained by fitting of the IR reflectivity spectra together with the THz experimental data (symbols) at temperatures below 450 K.

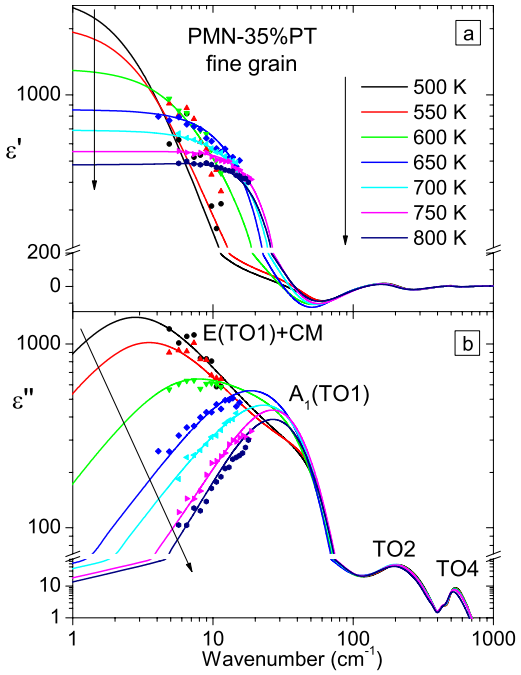

FIG. 10. (Color online) The same as in Fig. 9 for temperatures above 500 K.

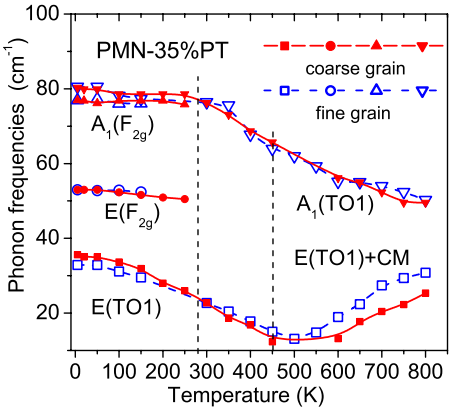

FIG. 11. (Color online) Components of the soft TO1 phonon mode. Temperature dependences of the A_1(TO1) and E(TO1) frequencies in the CGC (solid lines and symbols) and FGC (dash lines and open symbols) obtained from the multioscillator fits of the IR reflectivity spectra together with the THz data.

symmetry of PNC above T_C. The E(TO1) component is responsible for the increase in the reflectivity below 50 cm^{-1} and it is very well pronounced in the $\varepsilon''(\omega)$ spectra in Figs. 7 and 9. Note that the TO1 phonon splitting was never observed in Raman or INS spectra because the E component is highly damped, and therefore it is overlapped by central peak in both kinds of spectra. THz spectroscopy is more sensitive to overdamped excitations; therefore the splitting of the TO1 phonon was observed.

A_1(TO1) mode is underdamped ($\gamma_{TO} < 2\omega_{TO}$) below and overdamped ($\gamma_{TO} > 2\omega_{TO}$) above ~450 K in both ceramics. On lowering temperature the A_1(TO1) frequency increases from 52 cm^{-1} and saturates near 81 cm^{-1} below 250 K. Below the same temperature two new modes appear near 78 and 50 cm^{-1}. They presumably stem from the Raman-active mode of F_{2g} symmetry in the paraelectric phase, which activate in the FE phase below 250 K.

It is interesting to note that the A_1(TO1) phonon was recently investigated in PMN-PT single crystal by means of INS.[24] The authors found that, on cooling, the phonon hardens only below T_C while we see the hardening already below T_B. However, the TO1 phonon frequency cannot be directly determined from the INS at the Brillouin-zone center ($q = 0$) due to the above mentioned waterfall effect.[25] Its frequency is estimated only from the extrapolation of the optical phonon branch for $q \neq 0$.[24] On the other hand, IR spectroscopy can see just the long-wavelength polar phonons with $q \approx 0$ with higher resolution and accuracy than INS; therefore we trust more our IR and THz data..

TABLE I. Parameters of polar-phonon modes in fine grain ceramics. All the parameters are in cm^{-1}.

5 K				800 K			
ω_{TO}	γ_{TO}	ω_{LO}	γ_{LO}	ω_{TO}	γ_{TO}	ω_{LO}	γ_{LO}
32.9	44.8	46	35.8	30.8	77.4	49.5	224.8
53	15.4	54	15.9				
76.9	30.9	76.9	15.5				
80.6	20.7	103	26.9	50.3	96.8	117	37.5
105.8	29.4	125	26.3				
152	103.9	175.8	66.3				
211.8	69.8	291	212	209.5	143.8	286.3	262.8
292.9	87.5	334.9	96.2				
350.6	83.8	384.3	43.4	319.8	227.1	361.4	84.5
386.7	35	413.1	28.8	371.8	95.9	413.5	33.9
451.5	93.4	458.8	29.9	451.3	91.6	451.5	50.1
524.4	110.4	616	200.1				
620.1	93.9	714.3	52.3	492.7	156.6	703.3	58.6

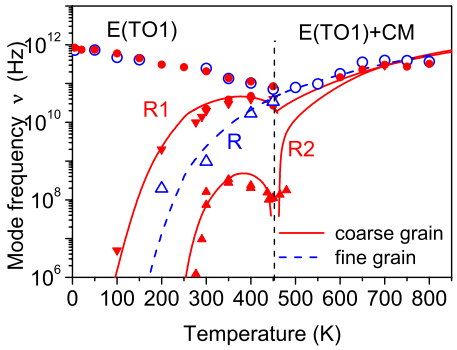

FIG. 12. (Color online) Soft and central modes in the CGC (solid lines and symbols) and FGC (dash lines and open symbols). Characteristic frequencies of the relaxational central mode components ($R1$,$R2$,R) and soft E(TO1) mode correspond to the maxima in the dielectric loss spectra. Symbols denote the experimental points, lines $R1$, $R2$, and R are fits of their temperature dependences (see details in the text).

The E(TO1) mode frequency behaves with temperature change similarly in both kinds of ceramics (Fig. 11) and exhibits minimum ($\omega_E \sim 14$ cm^{-1}) near 450 K, i.e., near T_C or T_m. Therefore it reminds the FE soft mode although the phase transition is not distinct in the dielectric data of FGC (Fig. 2).

The E(TO1) SM is mostly overdamped and, moreover, above room temperature it is overlapping with the relaxation mode (Fig. 12) describing the dynamics of PNC. While the A_1(TO1), TO2, and TO4 phonon contributions to ε' are moderate, the E(TO1) contribution is large and achieves (according to the IR and THz fits) more than 2000 between 450 and 600 K. Note that the static ε' is still several times higher due to the contribution of the relaxational modes (Figs. 4 and 5). The relaxation frequencies increase on heating, approach the THz range, and merge with the E(TO1) component at temperatures above $T_B \approx 600$ K. This is well known also from the pure PMN (Ref. 18) and other RFEs.[46] Therefore the overdamped feature seen above 300 K in the THz spectra below 1 THz should be assigned to the E mode overlapped with the relaxation. The relaxation is frequently called central mode (CM) since in inelastic-scattering experiments it appears as a central component of the spectra.

The fit parameters of an overdamped oscillator [Eq. (3)] are not unambiguous since the eigenfrequency ω_{SM} and damping γ_{SM} (hereafter we will speak only about the E component of the SM) are correlated, and a better physical meaning has the ratio

$$\omega_{SM}^2/\gamma_{SM} = \nu_{SM}, \tag{4}$$

which very approximately corresponds to the maximum of dielectric loss $\varepsilon''(\omega)$. We renormalized ω_{SM} seen in Fig. 11 using Eq. (4), transformed the frequency from cm^{-1} to Hz, and plotted it in Fig. 12 together with the mean relaxation frequencies $R1$, $R2$, and R corresponding to the experimental points of $\varepsilon''(f)$ maxima seen in Figs. 4 and 5.

Dielectric spectra of CGC clearly reveal two relaxation modes $R1$ and $R2$. Frequency of the high-frequency mode (ν_{R1}) increases quickly with temperature and arrives to the THz range near 300 K (see Figs. 7–10 and 12) while the low-frequency mode frequency (ν_{R2}) remains below 1 GHz at least until 500 K. Temperature dependence of $\nu_{R2}(T)$ does not follow a simple exponential law but shows an anomaly near T_C=440 K, which resembles a critical slowing down for the order-disorder ferroelectrics.[47,48] In addition, a quick exponential-like decrease in ν_{R2} appears on cooling in the FE phase below 350 K and reflects a freezing of the relaxation at finite temperatures far above 0 K.

Therefore, to describe the $\nu_{R2}(T)$, we combine the Vogel-Fulcher law usually used in the case of RFEs

$$\nu = \nu_0 \exp[-U/(T - T_{VF})], \tag{5}$$

and the critical slowing down[47,48]

$$\nu = A_1(T_C - T), \quad \text{at} \quad T < T_C, \tag{6a}$$

$$\nu = A_2(T - T_C), \quad \text{at} \quad T > T_C, \tag{6b}$$

where ν_0 is a high-temperature limit of the relaxation frequency, U and T_{VF} are the Vogel-Fulcher activation energy and temperature, respectively, and A_1 and A_2 are temperature independent constants.

Considering that the phase transition in CGC is of the first order, we derived the following equations with different parameters below and above T_C:

$$\nu_{R2} = A_1(T_1 - T)\exp[-U_1/(T - T_{VF1})] \quad \text{at} \quad T < T_C, \tag{7a}$$

$$\nu_{R2} = A_2(T - T_2)\exp[-U_2/(T - T_{VF2})], \quad \text{at} \quad T > T_C, \tag{7b}$$

where T_1, T_2 and T_{VF1}, T_{VF2} are the critical temperatures and Vogel-Fulcher temperatures, respectively, and U_1 and U_2 are the Vogel-Fulcher activation energies below and above T_C, respectively. Solid line $R2$ in Fig. 12 corresponds to the fit of $\nu_{R2}(T)$ with Eqs. (7a) and (7b) using parameters shown in Table II. One can see that combination of the critical slowing down and Vogel-Fulcher law describes well the experimental temperature dependence $\nu_{R2}(T)$. The critical temperatures T_1 and T_2, obtained from the fit, are close to T_C. The values of the Vogel-Fulcher temperature ($\sim$200 K) and activation energy ($\sim$700 K) are typical for PMN and other Pb-containing RFEs.[16,18]

Temperature dependence of $\nu_{R1}(T)$ reflects the relaxation freezing at temperatures close to 0 K and follows rather the Arrhenius than Vogel-Fulcher law but also shows an anomaly near T_C (see curve $R1$ at Fig. 12). To describe the $\nu_{R1}(T)$, we combine the Arrhenius law,

$$\nu = \nu_0 \exp[-E/T], \tag{8}$$

with the critical slowing down [Eq. (6)] and fit $\nu_{R1}(T)$ with the following equations:

$$\nu_{R1} = A_1(T_1 - T)\exp[-E_1/T], \quad \text{at} \quad T < T_C, \tag{9a}$$

$$\nu_{R1} = A_2(T - T_2)\exp[-E_2/T], \quad \text{at} \quad T > T_C, \tag{9b}$$

where ν_0 is the high-temperature limit of the relaxation frequency, and E, E_1, and E_2 are the Arrhenius activation ener-

TABLE II. Fit parameters of the temperature dependences of relaxation frequencies in CGS and FGS.

		Critical slowing down		Vogel-Fulcher law		Arrhenius law	
Relaxation frequency	Temperature range (Equation)	A_1 , A_2 [GHz/K]	T_1 , T_2 [K]	U_1 , U_2 [K]	T_{VF1} , T_{VF2} [K]	ν_0 [THz]	E_1 , E_2 [K]
ν_{R1} CGC	Below T_C	25	478				1500
	Above T_C	9	400				1500
ν_{R2} CGC	Below T_C [Eq. (6a)]	0.3	447	700	190		
	Above T_C [Eq. (6b)]	6	463	700	210		
ν_R FGC	Whole range					14	2600

gies. The fit parameters are shown in Table II.

The observed combinations of the critical slowing down with the Arrhenius or Vogel-Fulcher temperature dependence of ν_{R1} and ν_{R2} reflect the coexistence of the FE transition and relaxor behavior in CGC. The facts that activation energies are the same below and above T_C ($U_1=U_2=700$ K, $E_1=E_2=1500$ K), and Vogel-Fulcher temperatures are very similar (T_{VF1}, $T_{VF2}\sim 200$ K) show that the relaxor behavior takes place not only above but also below T_C. Similar to PMN,[18] $R1$ and $R2$ can be attributed to the dynamics of polar nanoclusters. The dominant mechanisms of this dynamics are dipole reversal (flipping) of PNC and fluctuations of PNC volume (breathing). Presumably, the MW and THz dispersion at high temperatures close to T_B is prevailingly due to the cluster dipole flipping. The interactions among polar clusters cause freezing (at least, partial) of the local dipole moments when approaching the freezing temperature T_f), substantially suppressing cluster flipping in weak fields below T_f. Consequently, the breathing mechanism contribution to the dielectric response prevails below T_f and is responsible for the frequency-independent dielectric loss at low temperatures. In the case of PMN (Ref. 18) and PMT,[44] it was shown that the relaxation describing flipping follows the Vogel-Fulcher law while the breathing follows the Arrhenius law. In the framework of the PNC concept, $R2$ can be related to the cluster flipping and $R1$ to the cluster breathing mechanisms.

The FE transition in PMN-PT can be consequently considered as a result of a jumpwise increase in the size of some nanoclusters, i.e., percolation of some of the PNC into macroscopic domains below T_C. Such interpretation explains why the relaxations slow down only partially on cooling unlike in PMN and other RFE without macroscopic phase transitions.[10,15,16,18,44] In our samples the PNC dynamics contributes to the dielectric response even below T_C which means that obviously not all PNC have transformed into FE domains. Our result is supported by the piezoresponse force microscopy of PMN-20%PT single crystals, which actually observed "normal" FE domains into which nanodomains of opposite P_s orientation are embedded.[49]

Two-component relaxation was observed also in the Brillouin scattering study in the GHz and THz ranges.[50] The authors explained it by two types of dipole moment rotation in PNC. The fast relaxation was attributed to the 180° dipole flipping and the other one to the non-180° dipole flipping. In our opinion, the flipping is not probable at low temperatures in the FE phase, only the breathing (PNC-wall fluctuations) can be active in analogy to the well-known FE domain-wall dynamics. Therefore we see only one broad relaxation below 200 K due to the PNC breathing.

Coexistence of the FE domains and PNC in CGC below T_C (T_m) is also supported by the SHG experiment (Fig. 13). The SHG signal in CGC does not tend to saturate on cooling below T_C unlike in classical ferroelectrics[51] but increases linearly down to room temperature, probably due to additional contribution of PNC, whose concentration and/or volume increase below T_C. The SHG signal is relatively large in the FE phase and its sharp decrease on heating above ~440 K can be attributed to the first-order FE transition. The weak tail above T_C which disappears only near $T_B\sim 650$ K brings evidence for the presence of PNC in the cubic phase. Thus, the temperature evolution of the dielectric spectra as well as SHG signal indicates presence of polar nanoclusters in CGC both above and below T_C.

Temperature dependence of SHG signal in FGC (Fig. 13) shows no steplike changes but only a smooth gradual change in the slope near $T_C=440$ K. It is important to stress that the SHG signal in FGC above T_C is much higher than in CGC. It shows a higher concentration of PNC in macroscopically cubic FGC. Moreover, the SHG signal remains nonzero up to our highest investigated temperature 750 K (Fig. 13) which indicates that the Burns temperature in FGC is markedly higher than that in CGC. Enhanced stability of PNC in FGC

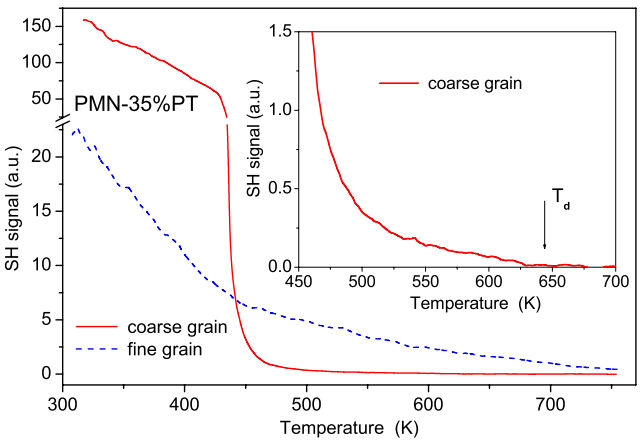

FIG. 13. (Color online) Temperature dependence of the SHG signal in CGC (solid lines) and FGC (dashed lines).

can be related to their reduced ability to flip under the applied electric field due to the pinning at grain boundaries. Below T_C the SHG signal in FGC is much smaller than in CGC, indicating a partial suppression of the FE domain growth. Nevertheless, the SHG intensity remarkably increases on cooling below T_C so that some smeared diffuse FE transition obviously still occurs in FGC. This is fully in agreement with previous work on analogous samples that showed submicron/nanometer sized crosshatched domains in the FGC sample and micron-sized lamellar domains in the CGC.[35]

Relaxational central mode component R in FGC is also attributed to the dynamics of PNC. Its mean frequency ν_R is related to superposition of both flipping and breathing mechanisms, which cannot be unambiguously separated from the spectra. This appears also due to a much smaller contribution of the PNC flipping, which is consequence of the above mentioned pinning of PNC on the grain boundaries. Temperature dependence of the relaxation frequency $\nu_R(T)$ (Fig. 12) follows roughly Arrhenius law (8) typical for a temperature activated process. The parameters of the fit are shown in Table II. No anomalies of $\nu_R(T)$ were observed near T_C. Nevertheless, similar to CGC, on cooling the relaxation does not shift below 1 MHz and gradually disappears from the spectra, which may be due to a percolation of PNCs into FE domains below T_C and freezing of their wall motion. It is seen that the cluster flipping strongly contributes to the permittivity in RFE crystals[18] and CGC; however in FGC, where the probability of PNC flipping is reduced, the permittivity is much lower (see Figs. 1 and 2).

Suppressing of the PNC flipping in FGC can also explain the Arrhenius behavior of $\nu_R(T)$. Usually in RFE where the flipping and breathing relaxations cannot be separated and create a broad dispersion band, the upper limit of the relaxation frequency distribution describes the breathing mechanism and follows the Arrhenius law while the lower limit describes the flipping mechanism and follows the Vogel-Fulcher law.[43,44,52] The mean relaxation frequency in this case also follows the Vogel-Fulcher law reflecting the major role of the PNC flipping mechanism. In contrary, Arrhenius behavior of $\nu_R(T)$, which is a mean relaxation frequency of the broad dispersion in FGC, evidences the reduced flipping and major role of the PNC breathing in FGC.

We also attempted to explain the difference in the dielectric dispersion of FGC and CGC (Figs. 4 and 5) by considering a reduced permittivity at grain boundaries (so-called dead layers). The grain size reduction results in increase in the relative dead-layer volume and the following reduction in the effective ε'. Such approach was successfully used to explain the suppressed effective ε' observed in $SrTiO_3$ ceramics and thin films.[6–8,53] We performed simulations according to the coated spheres (core-shell) model as in Refs. 54 and 55. If we consider the dielectric spectra of CGC as a bulk property of the cores and a small frequency-independent ε' as the property of the shells, the effective dielectric spectra of the core-shell composite still consisted of two well-separated relaxations. But the experimental spectra of FGC show only one smeared relaxation which is closer to $R1$ relaxation in CGC. While some effect of the lower ε' at the grain boundaries still cannot be excluded, it clearly shows that the main effect is suppression of the $R2$ relaxation connected with the PNC flipping due to their pinning by grain boundaries. Pinning of the PNC and blocking of the FE domain growth below T_C seems to be responsible for the dominance of the relaxor behavior in FGC.

Analyzing evolution of the PNC dynamics, beside T_B and T_f we should mention also the temperature T^* ($T_f < T^* < T_B$), where the dynamic PNC become quasistatic on cooling.[11,12,14] As the values of T_B and T_f in CGC are quite similar to those in PMN, one can expect also similar value of T^* [$\sim$400 K in PMN (Ref. 14)]. So, in CGC T^* should be close to T_C and the dynamics of PNC can transform directly to that of FE domains. It means T_C in PMN-xPT can be assigned as a percolation threshold of PNC into macroscopic ferroelectric domains. This picture is supported by the observed partial phonon softening near T_C indicating approaching to a local FE transition. This type of phase transition is neither clearly displacive nor order-disorder in a microscopic sense but concerns ordering on a mesoscopic range connected with partial phonon softening as well as partial critical slowing down of the relaxations. Such a type of phase transition was not yet discussed in the literature.

IV. CONCLUSIONS

In spite of some differences and peculiarities, $PbMg_{1/3}Nb_{2/3}O_3$-35%$PbTiO_3$ CGC and FGC have common features: similar phonon dynamics, existence of the relaxational dynamics of PNC, broad-frequency dielectric response, and temperature evolution of the local polarization demonstrated by the SHG experiment and characterized by a superposition of the relaxor behavior and the FE transition. In CGC, clear coexistence of the first-order FE transition near 440 K and relaxor behavior with the Burns temperature of $\sim$650 K was revealed. Reduction in the grain size in FGC resulted in weakening and smearing of the phase-transition features and domination of the relaxor behavior with higher estimated Burns temperature above 750 K.

In both ceramics, the lowest-frequency TO1 polar phonon is split for all temperatures below $\sim$800 K into the E and A_1 components due to a local dielectric anisotropy of PNC. Such splitting was never observed in INS or Raman-scattering spectra due to their lower resolution. The A_1 component hardens on cooling and saturates below T_{TR}. The E component lies below 1 THz at all temperatures, and softens down to $\sim$0.1 THz near T_C. Nevertheless, this softening is not responsible for the whole dielectric anomaly near T_C (or T_m) although it is apparently the driving force of the phase transition. The high value of the low-frequency permittivity is mainly caused by MW dielectric relaxation(s). The relaxation is split into two components in CGC. The lower-frequency component is assigned to flipping of PNC while the higher-frequency component to their breathing. The flipping relaxation frequency follows the Vogel-Fulcher law combined with a partial critical slowing down near T_C, and the breathing relaxation frequency follows the Arrhenius law combined with a small critical slowing down near T_C. Both relaxations are seen not only above T_C but also in the FE phase. It gives evidence, together with the temperature de-

pendence of SHG signal, about the coexistence of FE domains and PNC in the FE phase. In FGC the relaxation frequencies are overlapping and the lower-frequency relaxation is highly suppressed. The effective relaxation frequency follows the Arrhenius law without any anomaly near T_C and the breathing of PNC dominates in the dielectric response. It is presumably caused by pinning of PNC at grain boundaries.

The FE transition in PMN-PT appears as a percolation threshold of PNC into some macroscopic FE domains, triggered by softening of the lowest *E*-component TO phonon mode. This represents a unique type of crossover between the displacive and order-disorder phase transition, where the ordering process concerns a mesoscopic range.

ACKNOWLEDGMENTS

The authors acknowledge the support of the Czech Science Foundation (Projects No. 202/06/0403 and No. 202/09/0682) of the Academy of Sciences of the Czech Republic (Projects No. AVOZ 10100520 and No. KJB 100100704) and of the Ministry of Education (Contract No. COST-OC 101).

*kamba@fzu.cz

[1] C. Lichtensteiger, M. Dawber, and J.-M. Triscone, in *Physics of Ferroelectrics, A Modern Perspective*, edited by K. M. Rabe, C. H. Ahn, and J.-M. Triscone, (Springer-Verlag, Berlin, 2007), Chap. H, pp. 305–337.

[2] M. M. Saad, P. Baxter, R. M. Bowman, J. M. Gregg, F. D. Morrison, and J. F. Scott, J. Phys.: Condens. Matter **16**, L451 (2004).

[3] J. Junquera and Ph. Ghosez, Nature (London) **422**, 506 (2003).

[4] D. D. Fong, G. B. Stephenson, S. K. Streiffer, J. A. Eastman, O. Auciello, P. H. Fuoss, and C. Thompson, Science **304**, 1650 (2004).

[5] D. A. Tenne *et al.*, Science **313**, 1614 (2006).

[6] J. Petzelt *et al.*, Phys. Rev. B **64**, 184111 (2001).

[7] J. Petzelt, T. Ostapchuk, I. Gregora, P. Kuzel, J. Liu, and Z. Shen, J. Phys.: Condens. Matter **19**, 196222 (2007).

[8] J. Petzelt, T. Ostapchuk, I. Gregora, D. Nuzhnyy, I. Rychetský, K. Maca, and Z. Shen, Ferroelectrics **363**, 227 (2008).

[9] G. Burns and F. H. Dacol, Phys. Rev. B **28**, 2527 (1983).

[10] V. Bovtun, J. Petzelt, V. Porokhonskyy, S. Kamba, and Y. Yakimenko, J. Eur. Ceram. Soc. **21**, 1307 (2001).

[11] J. Toulouse, F. Jiang, O. Svitelskiy, W. Chen, and Z. G. Ye, Phys. Rev. B **72**, 184106 (2005).

[12] J. Toulouse, Ferroelectrics **369**, 203 (2008).

[13] J.-H. Ko, D. H. Kim, and S. Kojima, Phys. Rev. B **77**, 104110 (2008).

[14] E. Dul'kin, E. Mojaev, M. Roth, S. Kamba, and P. M. Vilarinho, J. Appl. Phys. **103**, 083542 (2008).

[15] A. A. Bokov and Z. G. Ye, J. Mater. Sci. **41**, 31 (2006).

[16] I. Rychetský, S. Kamba, V. Porokhonskyy, A. Pashkin, M. Savinov, V. Bovtun, J. Petzelt, M. Kosec, and M. Dressel, J. Phys.: Condens. Matter **15**, 6017 (2003).

[17] D. Viehland, M. Wuttig, and L. E. Cross, Ferroelectrics **120**, 71 (1991).

[18] V. Bovtun, S. Veljko, S. Kamba, J. Petzelt, S. Vakhrushev, Y. Yakymenko, K. Brinkman, and N. Setter, J. Eur. Ceram. Soc. **26**, 2867 (2006), and references therein.

[19] H. Ohwa, M. Iwata, H. Orihara, N. Yasuda, and Y. Ishibashi, J. Phys. Soc. Jpn. **70**, 3149 (2001).

[20] S. Kamba, E. Buixaderas, J. Petzelt, J. Fousek, J. Nosek, and P. Bridenbaugh, J. Appl. Phys. **93**, 933 (2003).

[21] A. Kania, Ph. Daniel, and A. Slodczyk, J. Phys.: Condens. Matter **18**, 9625 (2006).

[22] J.-Y. Sun, Y. Yang, K. Zhu, Y.-L. Liu, G. G. Siu, and Z. K. Xu, Chin. Phys. Lett. **25**, 290 (2008).

[23] S. Wakimoto, C. Stock, R. J. Birgeneau, Z.-G. Ye, W. Chen, W. J. L. Buyers, P. M. Gehring, and G. Shirane, Phys. Rev. B **65**, 172105 (2002).

[24] H. Cao, C. Stock, G. Xu, P. M. Gehring, J. Li, and D. Viehland, Phys. Rev. B **78**, 104103 (2008).

[25] J. Hlinka, S. Kamba, J. Petzelt, J. Kulda, C. A. Randall, and S. J. Zhang, Phys. Rev. Lett. **91**, 107602 (2003).

[26] S. E. Park and T. S. Shrout, J. Appl. Phys. **82**, 1804 (1997).

[27] B. Noheda, D. E. Cox, G. Shirane, S. E. Park, L. E. Cross, and Z. Zhong, Phys. Rev. Lett. **86**, 3891 (2001).

[28] H. Fu and R. E. Cohen, Nature (London) **403**, 281 (2000).

[29] G. A. Rossetti and A. G. Khachaturyan, Appl. Phys. Lett. **91**, 072909 (2007).

[30] W.-F. Rao and Yu. U. Wang, Appl. Phys. Lett. **92**, 102905 (2008).

[31] W. S. Chang, L. C. Lim, P. Yang, F.-T. Wang, C.-M. Hsieh, and C. S. Tu, J. Phys.: Condens. Matter **20**, 395229 (2008).

[32] P. Papet, J. P. Dougherty, and T. R. Shrout, J. Mater. Res. **5**, 2902 (1990).

[33] J. Carreaud, P. Geimeiner, J. M. Kiat, B. Dkhil, C. Bogicevic, T. Rojac, and B. Malic, Phys. Rev. B **72**, 174115 (2005).

[34] J. Carreaud, J. M. Kiat, B. Dkhil, M. Algueró, J. Ricote, R. Jiménez, J. Holc, and M. Kosec, Appl. Phys. Lett. **89**, 252906 (2006).

[35] M. Alguero, J. Ricote, R. Jiménez, P. Ramos, J. Carreaud, B. Dkhil, J. M. Kiat, J. Holc, and M. Kosec, Appl. Phys. Lett. **91**, 112905 (2007).

[36] R. Jiménez, H. Amorín, J. Ricote, J. Carreaud, J. M. Kiat, B. Dkhil, J. Holc, M. Kosec, and M. Algueró, Phys. Rev. B **78**, 094103 (2008).

[37] M. Alguero, A. Moure, L. Pardo, J. Holc, and M. Kosec, Acta Mater. **54**, 501 (2006).

[38] J. Krupka, T. Zychovicz, V. Bovtun, and S. Veljko, IEEE Trans. Ultrason. Ferroelectr. Freq. Control **53**, 1883 (2006).

[39] H. Okino, J. Sakamoto, and T. Yamamoto, Jpn. J. Appl. Phys., Part 1 **44**, 7160 (2005).

[40] V. Bovtun, S. Veljko, M. Savinov, A. Pashkin, S. Kamba, and J. Petzelt, Ferroelectrics **318**, 179 (2005).

[41] A. A. Bokov and Z.-G. Ye, Phys. Rev. B **66**, 064103 (2002).

[42] J. Hlinka, T. Ostapchuk, D. Noujni, S. Kamba, and J. Petzelt, Phys. Rev. Lett. **96**, 027601 (2006).

[43] J. Macutkevic, S. Kamba, J. Banys, A. Brilingas, A. Pashkin, J. Petzelt, K. Bormanis, and A. Sternberg, Phys. Rev. B **74**,

104106 (2006).
[44] S. Kamba, D. Nuzhnyy, S. Veljko, V. Bovtun, J. Petzelt, Y. L. Wang, N. Setter, J. Levoska, M. Tyunina, J. Macutkevic, and J. Banys, J. Appl. Phys. **102**, 074106 (2007).
[45] J. T. Last, Phys. Rev. **105**, 1740 (1957).
[46] J. Hlinka, J. Petzelt, S. Kamba, D. Noujni, and T. Ostapchuk, Phase Transitions **79**, 41 (2006).
[47] R. Blinc and B. Žekš, *Soft Modes in Ferroelectrics and Antiferroelectrics* (North Holland, Amsterdam, 1974).
[48] J. Petzelt, G. V. Kozlov, and A. A. Volkov, Ferroelectrics **73**, 101 (1987).
[49] V. V. Shvartsman and A. L. Kholkin, Phys. Rev. B **69**, 014102 (2004).
[50] S. Tsukada, Y. Ike, J. Kano, T. Sekiya, Y. Shimojo, R. Wang, and S. Kojima, Jpn. J. Appl. Phys., Part 1 **46**, 7151 (2007).
[51] R. C. Miller, Phys. Rev. **134**, A1313 (1964).
[52] S. Kamba, V. Bovtun, J. Petzelt, I. Rychetský, R. Mizaras, A. Brilingas, J. Banys, J. Grigas, and M. Kosec, J. Phys.: Condens. Matter **12**, 497 (2000).
[53] T. Ostapchuk, J. Petzelt, V. Železný, A. Pashkin, J. Pokorny, I. Drbohlav, R. Kužel, D. Rafaja, B. P. Gorshunov, M. Dressel, Ch. Ohly, S. Hoffmann-Eifert, and R. Waser, Phys. Rev. B **66**, 235406 (2002).
[54] I. Rychetský, J. Petzelt, and T. Ostapchuk, Appl. Phys. Lett. **81**, 4224 (2002).
[55] I. Rychetský and J. Petzelt, Ferroelectrics **333**, 227 (2006).